The vibrational spectra of a model boron dipyrromethene molecule in condensed phase: Experimental and theoretical insights

Alessandro Feis [a], Cristina Gellini [a,*], Marco Pagliai [a], Marilena Ricci [a], Carlo Adamo [b], Ilaria Ciofini [b], Feven Alemu Korsaye [b], Michele Turelli [b]

[a] *Dipartimento di Chimica "Ugo Schiff", Università di Firenze, Via della Lastruccia 3-13, 50019, Sesto Fiorentino, (Firenze), Italy*
[b] *PSL University, École Nationale Supérieure de Chimie de Paris, Centre National de la Recherche Scientifique, Institute of Chemistry for Life and Health Sciences, 11, rue Pierre et Marie Curie, F-75005, Paris, France*

ARTICLE INFO

ABSTRACT

Boron dipyrromethene (BODIPY) derivatives are an important class of organic molecular dyes. Their chemical structure can be easily modified by synthetic methods, introducing various substituent groups on a tricyclic core that represents the characteristic unit of these compounds. As a consequence, BODIPY optical properties can be designed to tune their absorption and emission in an especially wide wavelength range. A large amount of experimental and computational studies has been performed to investigate the electronic excited states of many structurally different BODIPY dyes. On the other hand, vibrational properties are by far less known for these compounds. We have therefore measured detailed infrared and Raman spectra of a model compound, namely, a BODIPY derivative with four methyl groups and a phenyl ring as substituents. The experimental spectra of the solid sample have been contrasted with *ab initio* spectra computed at the CAM-B3LYP/6-31G+(d) level. Computations have been performed both for the isolated molecule and including the crystalline environment. In the latter case, better agreement has been observed. An assignment is proposed for the 123 vibrational modes. These results form the basis for further spectroscopic studies on complex BODIPY derivatives.

1. Introduction

Research on molecular dyes continuously brings novel and useful advancements in numerous fields of chemistry and biology. Among organic molecules, much interest is aroused by the boron dipyrromethene (BODIPY) tricyclic derivatives because of their fundamental and technological relevance [1,2]. Chemical modifications are more easily feasible in BODIPY dyes than in many other classes of organic molecules [3,4]. BODIPY dyes display favorable optical properties: their absorption and emission bands can be tuned in an extended wavelength range – even in the infrared (IR) region [5–7]. Moreover, the emission quantum yield from the lowest excited electronic state approaches unity in many BODIPY derivatives [8]. The favorable properties of BODIPY fluorophores – including the related aza-BODIPY dyes [9,10] – have been well assessed in years of analytical and bioanalytical studies [11,12]. On the other hand, the excited state dynamics of these dyes can be changed by chemical modifications in order to increase alternative, non-radiative

relaxation pathways [13,14]. This strategy has been employed to project BODIPY-based drugs for photothermal and photodynamic therapy [15, 16].

Besides fluorescence imaging, resonance Raman (RR) can be exploited for biomedical imaging as a diagnostic tool. In fact - while advantageous from many points of view - fluorescence is not a universal property of probe molecules. Besides the variability of quantum yield, the dependence on excitation wavelength may become an issue. On the other hand, the information content of Raman spectra is more extended than that associated to fluorescence spectra, as vibrational spectra are more detailed than electronic ones [17]. For this reason, the number of Raman reporter molecules, assisting fluorescent molecular probes in analysis and imaging, is steadily growing [18–21]. Versatility in bioanalytical applications can be added by surface enhanced Raman spectroscopy [22,23].

Notwithstanding the importance of BODIPY dyes, the vibrational characteristics of their ground state – and vibronic properties of their

---

excited states in consequence – are overlooked to a large extent. One of the reasons for the data insufficiency is connected to the high fluorescence yield that often makes the measurement of Raman spectra unpractical. In addition, the number of atoms of the tricyclic core and of the side substituents increases the nuclear degrees of freedom and complicates the description of vibrational modes. In an attempt to face these issues, we have considered 1,3,5,7-tetramethyl-8-phenyl-4,4-difluoroboradiazaindacene (PhPM) as a model molecule for this class of compounds. Fig. 1 shows the chemical formula of this molecule. It consists of a tricyclic core substituted by four methyl groups and a phenyl ring. PhPM is so representative of the BODIPY dyes that its electronic spectra are reported as introductory to the excited state properties of this class of compounds [24]. Moreover, it has been described as a fluorescent probe in a targeted investigation about fibril formation by a dipeptide [25]. PhPM derivatives have been employed as investigative tools to study the aggregation of an amyloid polypeptide [26].

In the present article, both experimental and computed vibrational spectra of PhPM are presented and discussed in detail. From the theoretical point of view, this molecule has been simulated both isolated and including the crystalline environment, thanks to a recently developed electrostatic embedding protocol, enabling to consider the effect of the condensed phase on local properties [27,28]. By comparing the computed and observed spectra, the vibrational assignment has been performed, enabling a fine description of the vibrational signature of this model compound.

2. Materials and methods

2.1. Spectroscopy

PhPM (purity 97 %) has been purchased by Sigma Aldrich. KBr (purity 99 %) has been purchased by Merck. IR spectra of PhPM have been measured as KBr pellet solid sample, with a Shimadzu IR Affinity-1S FTIR spectrometer. The Raman spectrum has been measured on KBr pellet with a Multiram Bruker interferometer equipped with 1064 nm excitation wavelength, a resolution 2 cm^{-1}, 30 mW excitation power and acquiring 2000 scans.
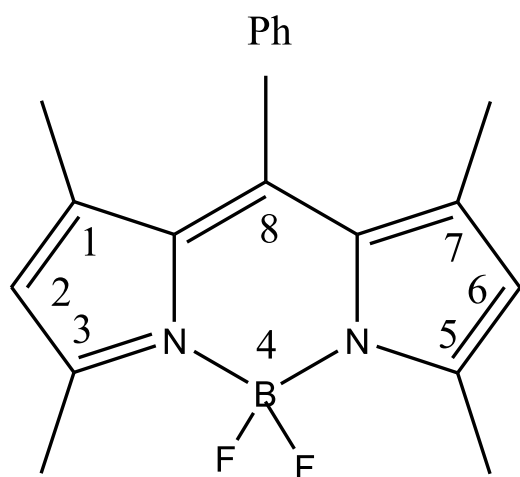

Fig. 1. Schematic structure of PhPM (CAS number: 194235-40-0) and corresponding labelling scheme. Methyl substituents are located at the 1, 3, 5, and 7 positions and a phenyl substituent at the 8 (*meso*) position.

2.2. Computational procedure

Density Functional Theory (DFT) has been applied both at the molecular and periodic level in order to simulate the structural properties of PhPM. With the aim of making these results a first step towards the understanding of ground to excited states vibronic coupling, we have applied an exchange and correlation functional, namely the range-separated hybrid CAM-B3LYP [29], which provides a reliable description of both ground and excited states of local and charge-transfer character [30,31]. Structural optimization of the isolated PhPM molecule has been performed by means of the Gaussian code [32] using the 6-31+G(d) basis set and has been followed by a harmonic frequencies calculation. These results are those considered in the discussion of the isolated molecule vibrational spectra.

The challenging task of simulating the effects of the local environment in the aggregated (crystalline) phase has been achieved by means of periodic DFT calculations, performed with CRYSTAL17 code [33,34], combined with calculations on a PhPM molecule embedded in the crystalline environment.

Periodic calculations have been performed starting from the crystal structure available for the PhPM molecule [35]. Experimentally, the PhPM molecule crystallizes in the *Pbca* space group. Both cell parameters and atomic positions have been optimized using the default convergence criteria of CRYSTAL17 for both self-consistent procedure and geometry optimizations (i.e. forces and displacements) using the B3LYP functional with empirical dispersion corrections. These periodic calculations have been performed using a 6-31G+(d) basis set optimized for organic materials in solid state [36].

A minimal representation of the crystal structure has been achieved by using the Ewald embedding procedure starting from the optimized periodic structure, with the aim of reducing the complexity of the final model as much as possible [27,28,37,38]. The information about the crystalline environment is encoded in a distribution of point charges able to reproduce the most relevant, i.e. electrostatic, effect. The ideal infinite lattice is actually reduced to a finite-sized volume populated by the point charges located at the crystal atomic positions. The system is partitioned into three concentric regions. The central region – zone I - contains the spectroscopically relevant system (i.e. a single PhPM molecule) and it is surrounded by a minimal model of the crystal lattice built from the Hirschfeld charges of each atom obtained from a population analysis performed with CRYSTAL17. The size of this region - zone II - can be controlled to adjust the embedding. The third region - zone III - surrounds the two previous ones and is populated by charges placed again according to lattice positions, whose value is fit in order to yield the Ewald potential of the infinite crystal in zone I and zone II. In our simulations 9245 fixed Hirschfeld charges have been used in zone II while 197112 charges have been fitted in zone III. The quality of the charge-fitting has been checked by calculating the root-mean square deviations between the direct Coulomb sum potential and the exact Ewald potential for 1000 sites randomly chosen in zone I and zone II. In our case, a mean root-mean square value of 1.6 μV has been obtained, thus allowing to evaluate the good accuracy of the embedding procedure.

Optimization and vibrational frequency of the aforementioned model (embedded molecule) have been next carried out with Gaussian16 [32] using the CAM-B3LYP functional and the 6-31G+(d) basis. Although harmonic vibrational frequencies can also be directly computed for the fully periodic system using the CRYSTAL17 code, the embedded cluster procedure has been preferred and applied since it is computationally less demanding and can be extended straightforwardly to the description of vibrational properties at the excited state.

For comparison with the experimental data, Raman intensities have been obtained from the computed Raman activities, using the relationship [39–41]:

$$I_i = \frac{f(\bar{\nu}_0 - \bar{\nu}_i)^4 A_i}{\bar{\nu}_i \left[1 - \exp\left(-\frac{hc\,\bar{\nu}_i}{k_B T}\right)\right]}$$

where I_i and A_i are the intensity and activity of the vibrational mode i, respectively; $\bar{\nu}_0$ is the exciting wavenumber (9398.5 cm^{-1}); $\bar{\nu}_i$ is the vibrational wavenumber of the i-th normal mode (in cm^{-1}); h, c, and k_B are fundamental constants, and f is a normalization factor for all peak intensities. Temperature effects have been considered setting T = 298.15 K. The calculated spectra have been reported by assigning to each normal mode a Lorentzian shape with a 10 cm^{-1} full width at half-maximum. The vibrational wavenumbers have been scaled by a 0.955 factor, matching the experimental wavenumber at 1434 cm^{-1} [42]. Finally, for comparison with the experimental IR spectrum, the calculated intensities, that scale with the natural logarithmic absorbance, have been converted to decadic logarithmic absorbance and then to % transmittance considering the usual exponential relation.

The assignment of the normal modes has been performed by inspection of the corresponding atomic displacements visualized using the GaussView software [32].

3. Results and discussion

3.1. Calculated structural properties of PhPM

The structural optimization performed on the PhPM isolated molecule indicates the C_{2v} geometry as the most stable (i.e. all vibrational frequencies are real [43]). The structure of PhPM is characterized by the

Table 1
– Calculated bond lengths (Ångström) and angles (degree, absolute values) of isolated PhPM and of PhPM in crystals. Experimental crystallographic data from the Supplementary files of Ref. [35] are also reported for comparison. Atomic numbering refers to Fig. 1.

Bonds and angles	Computed, isolated	Computed, embedded	Experimental, X-ray [35]
C$_1$–C$_2$	1.386	1.385	1.377
C$_2$–C$_3$	1.406	1.407	1.389
C$_3$–N$_{3a}$	1.339	1.340	1.348
N$_{3a}$–C$_{8a}$	1.398	1.401	1.403
N$_{3a}$–B$_4$	1.547	1.547	1.540
B$_4$–N$_{4a}$	1.547	1.542	1.546
N$_{4a}$-C$_5$	1.339	1.343	1.348
C$_5$–C$_6$	1.406	1.404	1.391
C$_6$–C$_7$	1.386	1.389	1.376
C$_7$–C$_{7a}$	1.428	1.425	1.420
C$_{7a}$-N$_{4a}$	1.398	1.400	1.399
C$_{7a}$-C$_8$	1.398	1.401	1.401
C$_8$–C$_{8a}$	1.398	1.398	1.394
C$_{8a}$-C$_1$	1.428	1.429	1.423
1-2-3	108.5	108.6	109.1
2-3-3a	109.0	109.0	108.8
3-3a-4	125.6	126.1	126.3
3a-4-4a	106.8	107.3	106.7
4-4a-5	125.6	125.7	126.3
4a-5-6	109.0	108.9	108.8
5-6-7	108.5	108.6	109.6
6-7-7a	106.0	105.9	105.6
7-7a-8	131.9	131.8	131.7
7a-8-8a	121.2	121.0	121.0
8-8a-1	131.9	131.7	131.8
1-2-3-3a	180.0	179.6	179.5
2-3-3a-4	180.0	174.5	176.0
3-3a-4-4a	180.0	178.9	179.8
3a-4-4a-5	180.0	177.1	177.7
4-4a-5-6	180.0	177.4	175.9
4a-5-6-7	180.0	179.8	179.9
5-6-7-7a	180.0	179.5	179.1
6-7-7a-8	180.0	179.9	177.7
7-7a-8-1	180.0	178.2	177.6
phenyl tilt	90.0	77.2	85.3

planarity of the tricyclic core and by the typical alternating single-/double C–C bond lengths in the pyrrole rings, as shown in Table 1. The structural parameters calculated on the isolated molecule are presented and compared with the experimental values obtained by X-ray diffraction [35]. Most structural features are common to other BODIPY dyes [44–46].

The presence at 8 position of the phenyl substituent does not affect the planarity of the tricyclic core of the isolated molecule, the phenyl ring being oriented perpendicularly to the skeleton backbone, as shown in the left panel of Fig. 2.

In the structure calculated for the embedded molecule, the tricyclic core is slightly distorted from planarity and the phenyl substituent is tilted by 77.2° with respect to the mean molecular plane as shown in the right panel of Fig. 2. These features lower the molecular symmetry and are in agreement with the observed crystal structure. We note that both the non-planarity of the crystal molecular unit and the variation of the phenyl tilt angle can only be correctly reproduced when the crystalline environment is included in our model.

3.2. Calculated vibrational spectra of PhPM

The PhPM molecule numbers 43 atoms. Therefore, 123 normal modes of vibration can be calculated, all of them potentially giving rise to both Raman and IR bands. In fact, the preceding section shows that the molecular symmetry is lowered for PhPM in the environment of the crystal. Therefore, a high degree of correspondence can be expected between the Raman and IR spectra of PhPM solids. In both measurements, crowded vibrational spectra are foreseen with relative intensities depending on the spectroscopic method.

It is useful to compare the spectra computed for both the isolated and the embedded molecule, before considering the relationship with the experimental spectra. The computed spectral data is shown in Figs. 3 and 4, in the form of bar graphs, while the numeric entries are reported in Table SM 1 in the Supplementary Materials section. This choice is potentially useful to benchmark the experimental spectra that will be shown in Subsection 3.3. An overall issue is the correspondence between the bands that are calculated in the case of isolated and embedded molecule. A first approach consists in tracing this correspondence through wavenumber and intensity similarities. To deepen the information that can be extracted by the calculations, we examined the mode composition by visual inspection of normal modes associated with each vibration. With a limited number of exceptions, we could track the vibrational modes that are common to PhPM in both environments. The wavenumber difference is generally small, namely, it does not exceed 2 % if only the region above 150 cm^{-1} is considered. The intensity is partially redistributed in both IR and Raman sets, although the overall intensity distribution of the spectra is not deeply changed by the embedding procedure. In agreement with symmetry lowering, a number of modes that are forbidden for the isolated molecule, namely, the A$_2$ modes in the IR spectra (e.g., those at 797 and 842 cm^{-1}), become allowed for the embedded molecule. These results are in line with previous calculations of vibrational spectra performed with related embedding methods in solutions [47] and molecular crystals [48]. As already stated, embedding does not deeply alter the spectra. The most representative changes in the lower-frequency region of the computed Raman spectra in Fig. 3 are the activity enhancement of the 366/400 cm^{-1} pair and that of the bands at 797 and 842 cm^{-1} (isolated molecule wavenumbers). More subtle changes can only be detected by a comparison between computed and experimental spectra, as it will be shown in the following. In the higher-frequency region, the activity of the 1119, 1416 and 1435 cm^{-1} bands is significantly increased. Spectral congestion makes other changes less clear, especially above 2900 cm^{-1}.

Significant spectral changes are brought by the embedding procedure in the computed IR spectra shown in Fig. 4. The intense band at 1062 cm^{-1} in the isolated molecule is shifted to 1046 cm^{-1}. Band multiplicity is especially increased around 800 cm^{-1} and between 1400
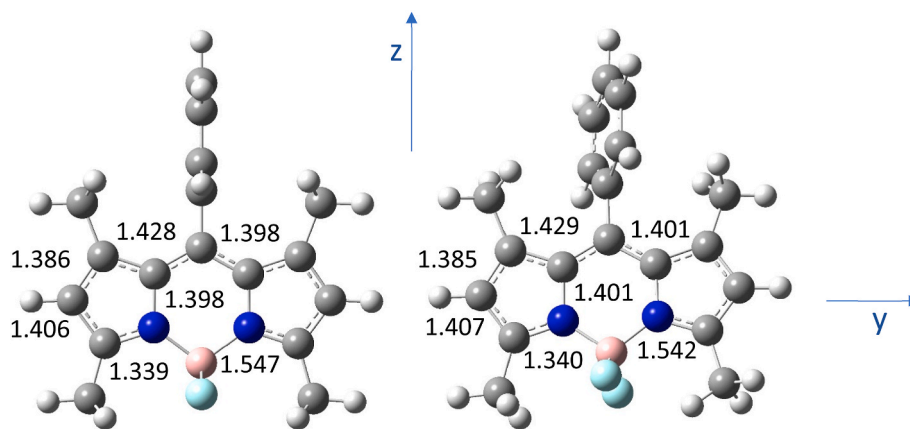
Fig. 2. – Schematic representation of the optimized structure of PhPM as isolated molecule (left) and in the crystalline environment (right). Selected bond lengths (in Å) are indicated together with two reference axes.

Fig. 3. – Computed Raman spectra of (a) isolated and (b) embedded PhPM. The data is extracted from Table SM 1 in order to facilitate the comparison. Please note that the activity of some bands does not fit into the ordinate scale. For these modes the activity is indicated as numbers above their peaks.
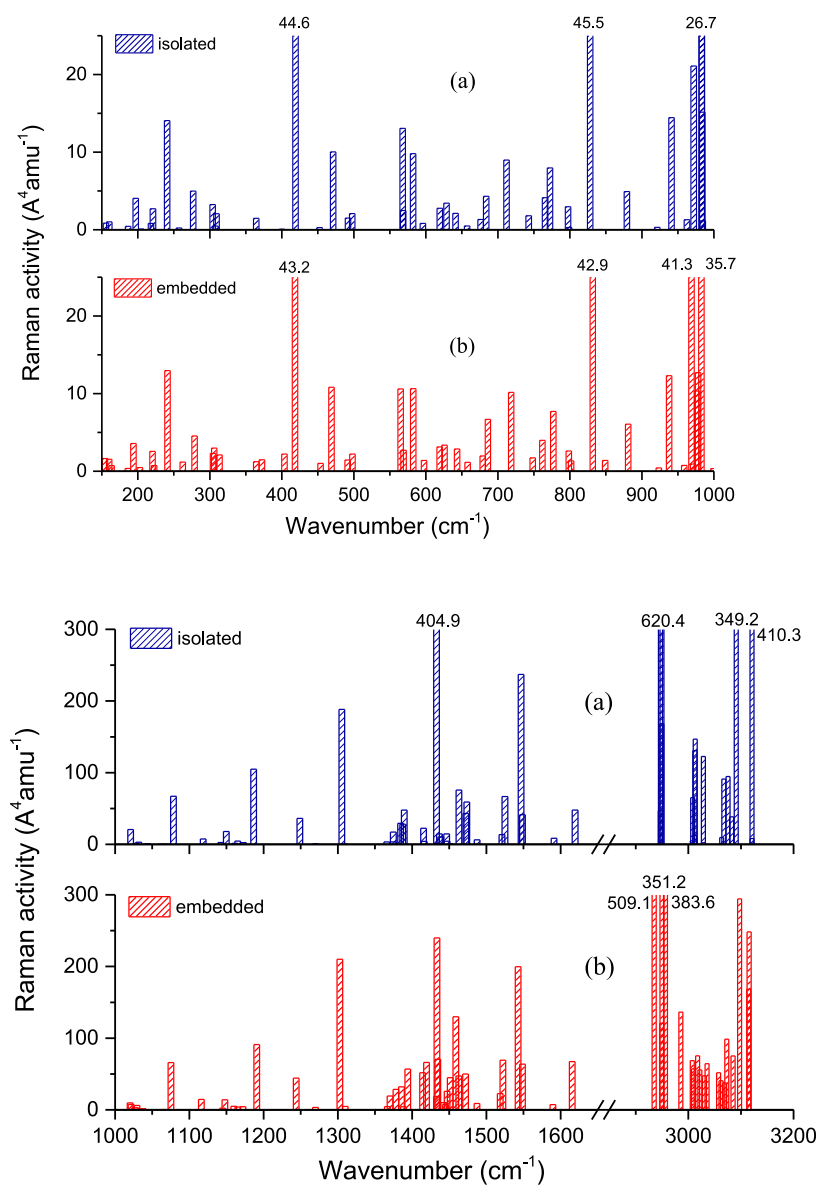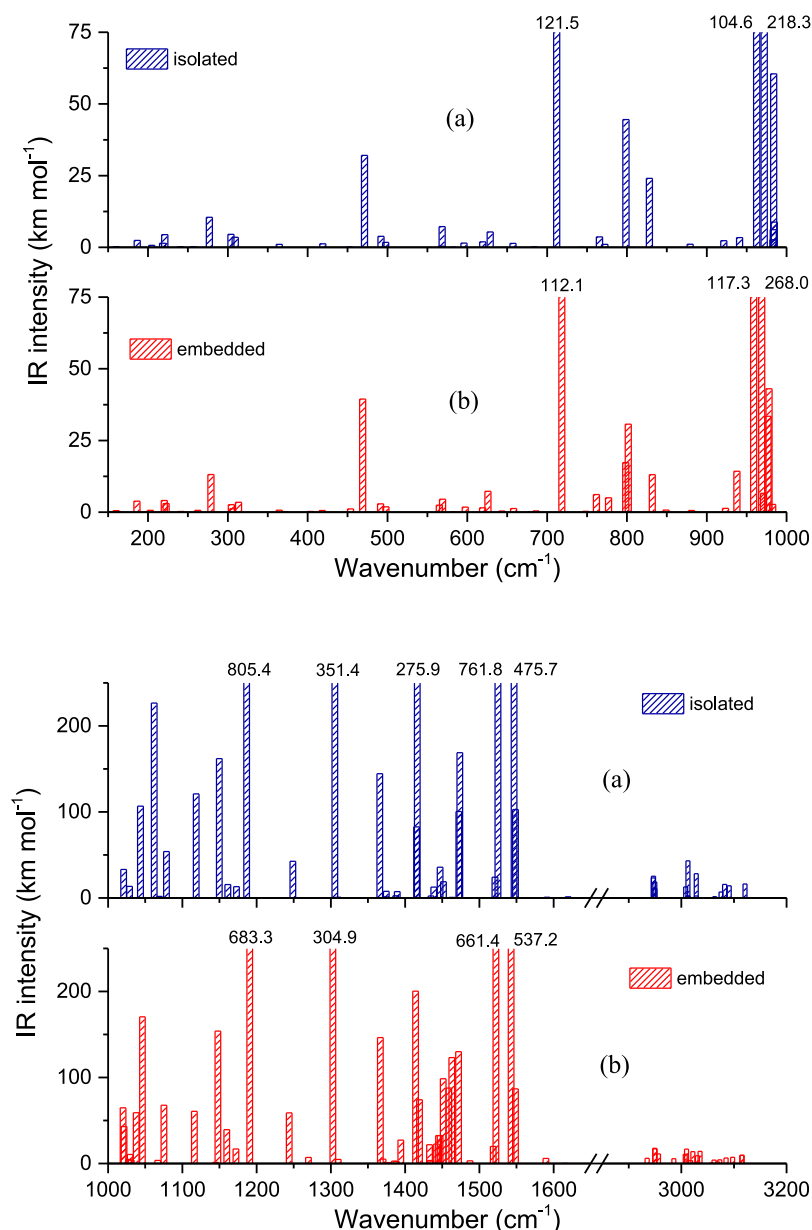
Fig. 4. – Computed IR spectra of (a) isolated and (b) embedded PhPM. The data is extracted from Table SM 1 in order to facilitate the comparison. Please note that the intensity of some bands does not fit into the ordinate scale. For these modes the intensity is indicated as numbers above their peaks.

and 1650 cm^{-1}. The region beyond 2900 cm^{-1} is characterized by minimal wavenumber differences between the bands of isolated and embedded molecule. The intensity, though, is largely redistributed. For clarity, in Figure SM 1 a graphic representation of the most intense vibrational modes is given.

3.3. Experimental Raman and IR spectra of PhPM

The experimental Raman spectrum of solid PhPM is shown in Fig. 5 together with the corresponding IR spectrum. The Raman spectrum is dominated by the two most intense bands at 428 and 1434 cm^{-1}. In addition, a large number of medium intensity bands are observed in the wavenumber region between 900 and 1700 cm^{-1}. They often appear as due to the superposition of more than one band as in the case of the doublets 1184/1196, 1464/1474, 1513/1519 and 1537/1545 cm^{-1}, or in the case of the multiplet around 1380 cm^{-1}. In this spectral region,

the highest observed wavenumber is 1605 cm^{-1}. Below 1000 cm^{-1} the average intensity decreases, whereas the Raman spectrum maintains its crowded appearance. Around 980 cm^{-1}, three overlapping bands are found at 984, 1000 and 1007 cm^{-1}. Sharp peaks are observed at 235, 477, 728, and 954 cm^{-1}, and doublets of comparable intensity at 780/788 and 585/600 cm^{-1}. Finally, two groups of bands are found in the high frequency region, namely, the doublet at 2929/2969 cm^{-1} and the weaker band group beyond 3000 cm^{-1}. The available instrumentation allowed us to detect a total amount of 75 Raman bands.

We turn now to the IR spectrum. Many of the low-intensity Raman bands are prominent in the IR spectrum, as in the case of the 721 and 1154 cm^{-1} bands. Moreover, the 972/980 cm^{-1} doublet and the one at 1184/1196 cm^{-1} dominate the intermediate wavenumber range together with strong bands at 1304, 1508, and 1539/1545 cm^{-1}. The IR intensity in the high frequency region is very weak. It is possible, though, to detect at least eight bands. In conclusion, the experimental
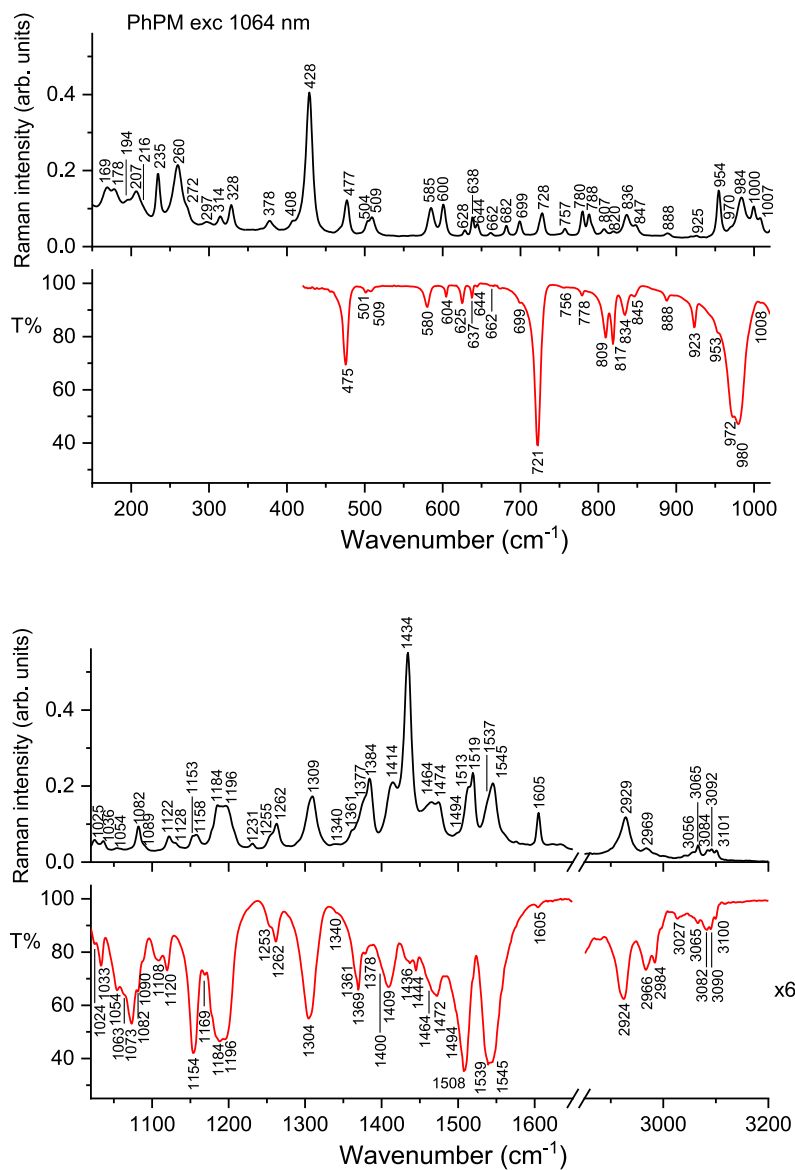
Fig. 5. Upper panels: Raman spectrum of solid (KBr pellet) PhPM. Excitation wavelength 1064 nm. Lower panels: IR transmittance spectrum of PhPM as KBr pellet solid sample.

data includes 86 vibrational bands if we consider both methods jointly. This compares favorably with the 123 predicted modes.

3.4. Vibrational assignment

Figs. 6 and 7 show the comparison between the experimental and calculated Raman spectra and that between the experimental and calculated IR spectra, respectively. Only the calculated spectra of the embedded molecule are displayed in these figures for clarity. There are two reasons for this choice. First, the experimental work was performed on crystalline samples, that are described by the embedding procedure more realistically. Moreover, as it will be explained in the detailed description, some features of the experimental spectra are only reproduced by the calculations performed for the embedded molecule. A general agreement in the band positions is observed when the appropriate scaling factor for wavenumbers is considered. Moreover, the calculated intensities, obtained as reported in Subsection 2.2, fit the experimental spectra to a large extent.

The comparison between experimental and computed spectra is displayed in Table 2, where an approximate mode description is also given. The region below 900 cm^{-1} is dominated by several torsional modes of the tricyclic core. In fact, more than ten Raman bands - experimentally observed and computationally predicted - receive a strong contribution from this kind of motion. The assignment accords with that proposed for an unsubstituted BODIPY dye [49]. In this region, additional torsional modes involve the five side groups: ten Raman bands correspond to modes involving the phenyl ring, whereas four low-frequency Raman bands are related to methyl torsions. All these mentioned bands are detected in the experimental Raman spectra notwithstanding their weak intensity. The intense IR band at 721 cm^{-1} is equally assigned to a phenyl torsion mode. A group of intense Raman bands involves methyl bending displacements, namely, the bands observed at 260, 428, 477 (possibly related to the same bending mode giving rise to the strong IR band observed at 475 cm^{-1}) and 600 cm^{-1}. Bending of the BF$_2$ moiety also contributes to medium-intensity Raman bands in this region, namely, those at 328, 504 and 585 cm^{-1}. Besides
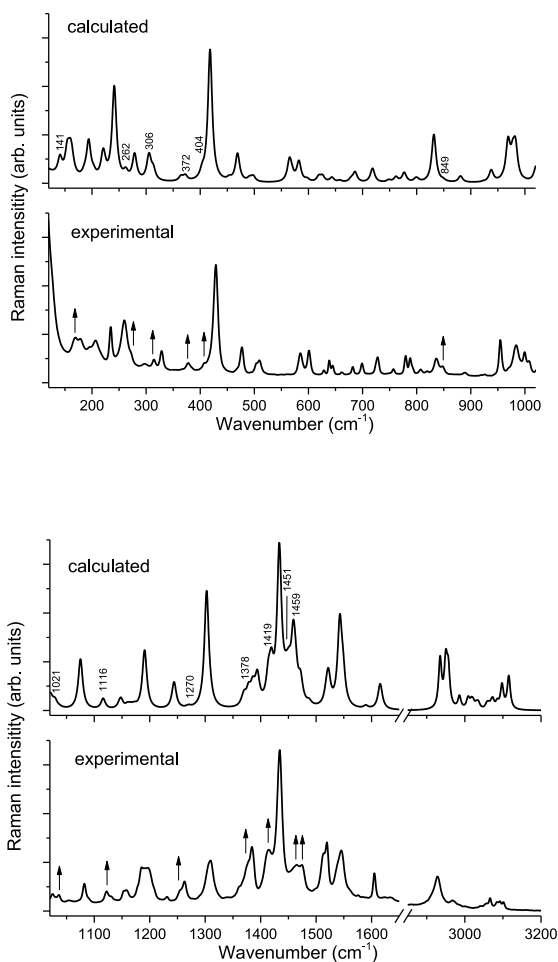
Fig. 6. – Calculated Raman spectrum of the embedded PhPM molecule and experimental Raman spectrum of solid PhPM in KBr pellet from Fig. 5. The arrows mark those bands that are enhanced according to the calculated intensities for embedded molecules.
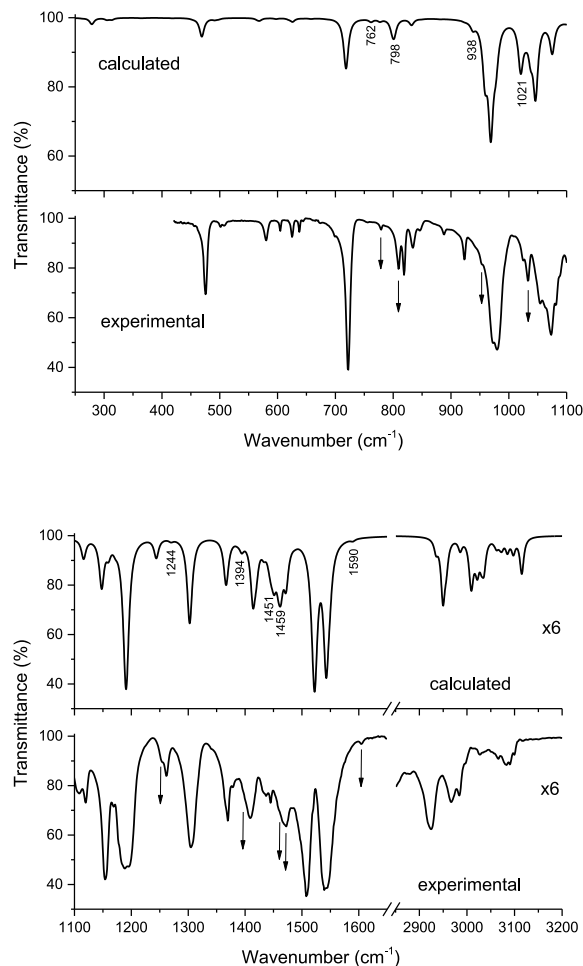

Fig. 7. – Calculated IR spectrum of the embedded PhPM molecule and experimental IR spectrum of solid PhPM from Fig. 5. The arrows mark those bands that are enhanced according to the calculated intensities for embedded molecules.

torsion and bending modes, some stretching modes are proposed in the assignment of the bands below 900 cm^{-1}. These modes (e.g., the one predicted at 762 cm^{-1}) include displacements of the tricyclic core nuclei, including B and N, as well as CC stretching of the side methyl and phenyl groups. Some of them originate intense Raman bands: an outstanding example is that of the band at 428 cm^{-1} (experimental wavenumber). A group of six bands is predicted to be enhanced only for embedded molecules, e.g., the bands observed at 378 and 408 cm^{-1}. The intensity enhancement related to embedding is marked by arrows in Figs. 6 and 7.

The range between 900 and 1700 cm^{-1} displays additional complexity in the assignment, due to the large number of nuclear displacement contributions. Many normal modes involve bending of various CCH angles: this feature is common to many hydrocarbon molecules. More specific to PhPM is the BF stretching mode, that contributes to the calculated band doublet at 938 and 959 cm^{-1}. These two bands can be detected both in the Raman spectrum at 954 and 970 cm^{-1} and in the IR spectrum at 953 and 972 cm^{-1}. Several stretching modes are spread on the tricyclic core and can be related to intense bands, for instance, the very strong one predicted at 1303 cm^{-1} – observed at 1309 cm^{-1} in the Raman spectrum and at 1304 cm^{-1} in the IR spectrum – as well as to many bands in the 1200–1550 cm^{-1} range. In a few cases (namely, the bands predicted at 983, 1067, 1270, and 1590/1615 cm^{-1})

CC stretching modes are localized on the phenyl substituent instead. The intensity enhancement due to embedding is apparent for seven Raman bands and five IR bands in this range.

The 2900–3200 cm^{-1} range is assigned to manifold CH stretching modes. They can be qualitatively grouped into H atom displacements of the four methyl groups, of the phenyl ring, and of the two methine groups, in order of ascending wavenumber.

The Raman and IR spectra lead to a detailed description of the vibrational structure of the electronic ground state of this model molecule that significantly represents the large BODIPY dyes family. For instance, we assign the band predicted at 469 cm^{-1} to a mainly bending mode of the ring nuclei. The important role in vibronic coupling through a closely related vibration has been highlighted in the two-dimensional electronic spectra of a similar BODIPY dye [50], that bears a propionyl group in place of the phenyl ring of PhPM. The calculations previously performed for a tetramethyl BODIPY dye, equally missing the phenyl ring, yield very similar wavenumbers as in our case [51]. The comparison does not concern spectral intensities, as they are not quoted. On the other hand, the distribution among symmetry species of the C_{2v} group favorably compares with the prediction we present in Table SM 1 for the isolated PhPM molecule. Finally, we observe that the assignment we propose for PhPM can be related to an important recent investigation on RR spectroscopy and excited-state dynamics in a similar BODIPY dye

Table 2

– Experimental and calculated vibrational wavenumbers (cm^{-1}) of PhPM, together with calculated IR intensities (I_{IR}, km mol^{-1}) and Raman activities (I_R, Å^4 amu^{-1}). The approximate mode description is also indicated. Abbreviations: τ, torsion; δ, bending; ν, stretching; ip, in plane; sym, symmetric; asym, asymmetric; C_n indicates the C atoms numbered as in Fig. 1; C_{met} labels the C atom of the methyl groups; "ring" indicates modes of the tricyclic core. In parenthesis, calculated data referred to the isolated PhPM molecule are also reported.

PhPM experimental IR and Raman wavenumbers		Embedded PhPM: calculated wavenumbers, IR intensities and Raman activities			
IR	Raman	$\bar{\nu}$	I_{IR}	I_R	Approximate mode description
	169	141 (141)	0.8 (1.0)	0.95 (0.5)	τ (C C C_{met} H)
	178	164 (160)	0.1 (0.3)	0.7 (1.0)	δ (CNB) / δ (CCC)
	194	186 (186)	3.9 (2.4)	0.4 (0.4)	τ (ring CCCC) / τ (C C C_{met} H)
	207	194 (197)	0.0 (0.0)	3.6 (4.0)	τ (C C C_{met} H)
	216	203 (205)	0.6 (0.7)	0.5 (1.0)	τ (C C C_{met} H)
	235	220 (221)	4.1 (4.4)	2.6 (2.7)	δ (ring CCC)
		223 (218)	3.0 (1.4)	0.7 (0.8)	τ (phenyl CCCC) / δ (CNB)
	260	241 (241)	0.2 (0.2)	13.0 (14.0)	δ (C C C_{met})
	272	262 (257)	0.6 (0.2)	1.2 (0.2)	τ (phenyl CCCC)
	297	279 (277)	13.1 (10.5)	4.5 (5.0)	δ (C C C_{met})
	314	304 (304)	2.6 (4.5)	2.3 (3.2)	δ (N C C_{met}) / ν (NB)
		306 (308)	1.2 (0.0)	3.0 (0.5)	τ (ring CCCC)
	328	313 (309)	3.5 (3.5)	2.1 (2.0)	δ (FBF)
		364 (364)	0.7 (1.0)	1.2 (1.5)	τ (ring CCCC) / τ (CCCN)
	378	372 (366)	0.1 (0.0)	1.5 (0.0)	τ (CCNB) / τ (ring CCCH)
	408	404 (400)	0.2 (0.0)	2.2 (0.1)	τ (phenyl CCCH)
	428	418 (419)	0.6 (1.2)	43.2 (44.6)	ν (BN) / δ (C C C_{met})
		454 (452)	1.1 (0.1)	1.0 (0.3)	τ (CNBN) / τ (CCNB)
475	477	469 (471)	39.4 (32.0)	10.8 (10.0)	δ (C C C_{met}) ip / δ (NCC) / δ (CNB)
501	504	491 (492)	2.9 (3.8)	1.4 (1.5)	δ (FBF) / δ (C C C_{met})
509	509	498 (498)	1.9 (1.7)	2.2 (2.1)	τ (ring CCCC) / τ (phenyl CCCH)
	585	565 (568)	2.4 (0.4)	10.6 (13.1)	ν (C–CH$_3$) / δ (FBF) / δ (NBN)
580		569 (568)	4.5 (7.2)	2.7 (2.5)	ν (C–CH$_3$) / δ (ring CCC)
	600	582 (582)	0.1 (0.0)	10.6 (9.8)	ν (C–CH$_3$) / δ (C C C_{met}) / δ (CCN)
604		597 (596)	1.8 (1.5)	1.4 (0.2)	τ (CCCN)
625	628	619 (619)	1.5 (1.9)	3.1 (2.8)	τ (CCCN) / δ (phenyl CCC)
637	638	626 (628)	7.3 (5.4)	3.4 (3.4)	δ (phenyl CCC) / δ (ring CCC)
644	644	643 (641)	0.4 (0.0)	2.9 (2.1)	τ (CCCN) / τ (ring CCCC)
662	662	658 (657)	1.3 (1.4)	1.1 (0.5)	τ (CCNB) / τ (CCCN)

Table 2 (*continued*)

PhPM experimental IR and Raman wavenumbers		Embedded PhPM: calculated wavenumbers, IR intensities and Raman activities			
IR	Raman	$\bar{\nu}$	I_{IR}	I_R	Approximate mode description
699	699	679 (676)	0.2 (0.0)	2.0 (1.3)	τ (CCNB) / τ (CCCN)
	728	686 (684)	0.4 (0.2)	6.7 (4.3)	τ (ring CCCH) / τ (phenyl CCCC)
721		718 (712)	112.1 (121.5)	10.2 (9.0)	τ (phenyl CCCH)
756	757	748 (743)	0.3 (0.0)	1.7 (1.8)	τ (CCCN)
778	780	762 (766)	6.1 (3.6)	4.0 (4.1)	ν (phenyl CC) / ν (BF) / ν (C–CH$_3$) / δ (phenyl CCC)
	788	777 (772)	5.0 (1.0)	7.7 (8.0)	τ (ring CCCC) / τ (phenyl CCCH)
809	807	798 (797)	17.3 (0.0)	2.6 (3.0)	τ (ring CCCH)
817	820	802 (799)	30.7 (44.6)	1.3 (0.3)	τ (ring CCCH)
834	836	832 (828)	13.1 (24.0)	42.9 (45.5)	ν (BN) / ν (ring CC)
845	847	849 (842)	0.7 (0.0)	1.4 (0.0)	τ (phenyl CCCH) / τ (phenyl HCCH)
888	888	881 (879)	0.6 (1.1)	6.1 (4.9)	τ (phenyl CCCH) / ν (ring CC)
923	925	924 (921)	1.3 (2.3)	0.4 (0.3)	τ (phenyl CCCH)
953	954	938 (941)	14.2 (3.4)	12.3 (14.4)	ν (BF) / δ (ring CCC) / δ (FBF)
972	970	959 (962)	117.3 (104.6)	0.7 (1.3)	ν (BF) / δ (FBF)
980	984	969 (972)	268.0 (218.3)	41.3 (21.1)	δ (C C_{met} H)
		971 (965)	6.6 (0.0)	0.9 (0.0)	τ (phenyl HCCH)
		977 (984)	33.4 (60.5)	10.3 (15.1)	δ (ring CCH)
		978 (983)	43.0 (6.1)	12.7 (26.7)	δ (ring CCH)
	1000	983 (983)	2.7 (2.6)	35.5 (33.6)	ν (phenyl CC) / δ (phenyl CCC)
		999 (984)	0.1 (8.8)	0.4 (1.1)	τ (phenyl HCCH)
1033	1036	1020 (1021)	64.8 (33.0)	9.5 (20.6)	ν (phenyl CC) / δ (phenyl CCH)
		1021 (1028)	42.9 (0.3)	7.5 (0.0)	ν (BF) / δ (C C_{met} H)
1024	1025	1027 (1028)	4.7 (0.0)	2.9 (1.4)	τ (CCCH)
1054	1054	1029 (1029)	10.6 (13.4)	6.2 (0.2)	δ(C C_{met} H)
		1031 (1032)	4.0 (0.0)	0.9 (3.0)	τ (CCCH)
1063		1038 (1043)	59.0 (106.7)	1.6 (1.0)	δ(C C_{met} H)
1073		1046 (1062)	170.5 (226.6)	0.3 (0.2)	δ (C C_{met}t H) / ν (BF) / τ (BNCC$_7$)
1090	1089	1067 (1069)	3.6 (1.7)	0.3 (0.1)	ν (phenyl CC) / δ (phenyl CCH)
1082	1082	1075 (1078)	67.7 (53.9)	65.9 (67.1)	ν (BN) / ν (C–CH$_3$)
1108					
1120	1122	1116 (1119)	60.7 (120.9)	14.5 (7.4)	ν (BN) / ν (CN) / ν (CC)
	1128	1145 (1142)	1.3 (0.0)	2.4 (2.5)	δ (phenyl CCH) / ν (phenyl CC)
1154	1153	1148 (1150)	153.9 (162.0)	13.9 (17.8)	δ (ring CCH)

Table 2 (*continued*)

PhPM experimental IR and Raman wavenumbers		Embedded PhPM: calculated wavenumbers, IR intensities and Raman activities			
IR	Raman	$\bar{\nu}$	I_{IR}	I_R	Approximate mode description
1169		1160 (1161)	39.4 (15.6)	4.9 (1.4)	δ (ring CCH)
	1158	1165 (1165)	0.0 (0.0)	4.0 (4.6)	δ (phenyl CCH)
1184	1184	1172 (1173)	16.8 (13.2)	4.3 (2.4)	δ (phenyl CCH)
1196	1196	1191 (1186)	683.3 (805.4)	91.0 (104.8)	ν (CN) ν (BN) δ (C C$_{met}$ H)
	1231				
1262	1262	1244 (1249)	58.8 (42.7)	44.3 (36.2)	ν (CN) ν (C$_8$-phenyl C) ν (BN) δ (phenyl CCH)
1253	1255	1270 (1270)	7.0 (0.0)	3.3 (0.7)	ν (phenyl CC) δ (phenyl CCH)
1304	1309	1303 (1305)	304.9 (351.4)	210.1 (188.2)	ν (CC) ν (CN)
1340	1340	1310 (1310)	4.7 (0.8)	4.7 (0.4)	δ (phenyl CCH)
1369		1367 (1366)	146.3 (144.5)	4.4 (3.3)	ν (CN) ν (CC) δ (ring CCH) δ (H C$_{met}$ H)
1361	1361	1370 (1375)	5.1 (1.3)	19.3 (17.1)	ν (CC) δ (C C$_{met}$ H)
1378	1377	1378 (1375)	0.8 (7.6)	28.5 (3.4)	δ (H C$_{met}$H)
1400	1384	1386 (1384)	2.8 (0.3)	32.1 (29.4)	δ (H C$_{met}$H) δ (C C$_{met}$ H)
		1388 (1387)	2.2 (2.4)	4.4 (28.2)	δ (H C$_{met}$H)
		1394 (1389)	27.2 (7.3)	56.9 (47.8)	δ (H C$_{met}$H)
1409		1414 (1416)	200.3 (276.0)	51.7 (4.1)	ν (CN) δ (H C$_{met}$H)
	1414	1419 (1415)	74.0 (82.6)	66.0 (22.5)	δ (H C$_{met}$H)
	1434	1433 (1433)	3.5 (0.0)	239.7 (404.9)	ν (CC$_{met}$) δ (H C$_{met}$H) τ (C C$_{met}$ H) τ (N C$_{met}$ H)
1436		1433 (1437)	21.8 (0.0)	18.7 (14.5)	δ (H C$_{met}$H)
		1434 (1435)	3.4 (2.2)	70.3 (1.3)	δ (phenyl CCH) ν (phenyl CC)
1444		1442 (1438)	22.6 (12.7)	9.9 (10.2)	δ (H C$_{met}$H)
		1445 (1447)	32.5 (0.0)	7.7 (14.5)	δ (H C$_{met}$H)
		1447 (1447)	32.4 (35.8)	25.7 (4.3)	δ (H C$_{met}$H)
1464	1464	1451 (1452)	98.5 (18.9)	44.8 (1.0)	δ (H C$_{met}$H)
1472	1474	1459 (1463)	87.6 (0.6)	129.9 (75.7)	δ (H C$_{met}$H)
		1463 (1472)	123.1 (100.5)	47.2 (43.0)	δ (H C$_{met}$H) ν (CC)
1494	1494	1472 (1473)	130.0 (168.9)	50.0 (59.0)	δ (H C$_{met}$H) ν (CC)
		1487 (1487)	3.0 (0.1)	8.8 (6.2)	δ (phenyl CCH)
	1519	1519 (1521)	19.8 (24.1)	22.5 (13.6)	ν (CC) δ (ring CCH) δ (phenyl CCH)
1508	1513	1522 (1525)	661.4 (761.8)	69.2 (66.7)	ν (CN) ν (CC) ν (CC$_{met}$) δ (ring CCH)
1545	1545	1543 (1547)	537.2 (475.7)	199.7 (237.1)	ν (CC)
1539	1537	1549 (1549)	86.7 (102.8)	63.8 (41.2)	ν (CN) ν (CC) δ (ring CCH)
1605		1590 (1591)	5.9 (0.8)	7.3 (8.4)	ν (phenyl CC) δ (phenyl CCH)
	1605	1615 (1619)	0.1 (1.3)	67.2 (47.7)	ν (phenyl CC) δ (phenyl CCH)
2924	2929	2935 (2947)	6.1 (23.3)	509.1 (46.9)	ν (C$_{met}$-H) asym
2966	2969	2949 (2947)	17.6 (25.2)	120.7 (377.8)	ν (C$_{met}$-H) sym
2984		2950 (2949)	17.0 (18.6)	351.1 (168.3)	ν (C$_{met}$-H) asym
		2956 (2950)	11.2 (10.8)	383.6 (620.4)	ν (C$_{met}$-H) sym
		2986 (3007)	5.5 (0.0)	136.3 (4.9)	ν (C$_{met}$-H)
		3007 (3008)	10.6 (12.8)	68.7 (65.0)	ν (C$_{met}$-H)
		3010 (3012)	16.7 (0.0)	57.1 (12.1)	ν (C$_{met}$-H)
		3017 (3012)	3.5 (2.4)	75.3 (130.8)	ν (C$_{met}$-H)
		3022 (3013)	13.8 (43.1)	55.6 (0.0)	ν (C$_{met}$-H)
		3030 (3013)	9.0 (1.7)	47.3 (146.7)	ν (C$_{met}$-H)
		3036 (3028)	14.1 (28.2)	64.3 (2.1)	ν (C$_{met}$-H)
		3062 (3028)	3.9 (2.3)	40.6 (122.6)	ν (C$_{met}$-H)
3027	3056	3058 (3063)	0.7 (1.5)	51.8 (9.3)	ν (phenyl CH)
3065	3065	3069 (3067)	1.9 (0.2)	37.5 (91.1)	ν (phenyl CH)
3082	3084	3073 (3075)	4.2 (6.9)	98.5 (94.7)	ν (phenyl CH)
		3085 (3082)	6.4 (15.7)	75.1 (38.3)	ν (phenyl CH)
		3097 (3091)	7.2 (14.1)	294.2 (349.2)	ν (phenyl CH)
3090	3092	3115 (3121)	9.5 (16.2)	168.2 (8.0)	ν (ring CH) asym
3100	3101	3116 (3121)	9.6 (0.3)	248.2 (410.3)	ν (ring CH) sym

[52,53], that presents two ethyl substituents at the positions 2 and 6.

4. Conclusions

Both Raman and IR spectra have been measured and adequately computed for the model molecule PhPM. We have learnt that environmental effects should be included via an embedding procedure in the calculation to reach a better agreement with the experimental spectra in the solid state. Vibrational assignment shows that most modes are largely delocalized on the whole molecule. The impact of this description extends beyond the significance of PhPM, as the number of BODIPY molecules is steadily increasing. It can be foreseen that Raman reporters (i.e., molecules with intense Raman bands and tolerable fluorescence background) will be growingly demanded, especially for imaging applications in the near-infrared range [54].

CRediT authorship contribution statement

Alessandro Feis: Writing – original draft, Supervision, Methodology, Investigation, Formal analysis, Data curation, Conceptualization. **Cristina Gellini:** Writing – original draft, Supervision, Methodology, Investigation, Formal analysis, Data curation, Conceptualization. **Marco Pagliai:** Software. **Marilena Ricci:** Writing – original draft, Formal analysis, Data curation, Conceptualization. **Carlo Adamo:** Resources, Data curation. **Ilaria Ciofini:** Writing – original draft, Resources, Formal analysis, Data curation, Conceptualization. **Feven Alemu Korsaye:** Software. **Michele Turelli:** Software.

Declaration of competing interest

The authors declare that they have no known competing financial interests or personal relationships that could have appeared to influence the work reported in this paper.

Data availability

Data will be made available on request.

Appendix A. Supplementary data

Supplementary data to this article can be found online at https://doi.org/10.1016/j.dyepig.2024.112405.

References

[1] Cheng H-B, Cao X, Zhang S, Zhang K, Cheng Y, Wang J, Zhao J, Zhou L, Liang X-J, Yoon J. BODIPY as multifunctional theranostic reagent in biomedicine:Self-Assembly, properties and applications. Adv. Mater. 2023;35:2207546. https://doi.org/10.1002/adma.202207546.

[2] Wang S, Gai L, Chen Y, Ji X, Lu H, Guo Z. Mitochondria-targeted BODIPY dyes for small molecule recognition, bio-imaging and photodynamic therapy. Chem Soc Rev 2024. https://doi.org/10.1039/d3cs00456b.

[3] Boens N, Leen V, Dehaen W. Fluorescent indicators based on BODIPY. Chem Soc Rev 2012;41:1130–72. https://doi.org/10.1039/c1cs15132k.

[4] Boens N, Verbelen B, Ortiz MJ, Jiao L, Dehaen W. Synthesis of BODIPY dyes through postfunctionalization of the boron dipyrromethene core. Coord Chem Rev 2019;399:213024. https://doi.org/10.1016/j.ccr.2019.213024.

[5] Descalzo AB, Xu H-J, Shen Z, Rurack K. Red/Near-infrared boron–dipyrromethene dyes as strongly emitting fluorophores. Ann N Y Acad Sci 2008;1130:164–71. https://doi.org/10.1196/annals.1430.016.

[6] Yuan L, Lin W, Zheng K, He L, Huang W. Far-red to near infrared analyte-responsive fluorescent probes based on organic fluorophore platforms for fluorescence imaging. Chem Soc Rev 2013;42:622–61. https://doi.org/10.1039/c2cs35313j.

[7] Huang L, Han G. Near infrared boron dipyrromethene nanoparticles for optotheranostics. Small Methods 2018;2:1700370. https://doi.org/10.1002/smtd.201700370.

[8] Bumagina NA, Antina EV, Ksenofontov AA, Antina LA, Kalyagin AA, Berezin MB. Basic structural modifications for improving the practical properties of BODIPY. Coord Chem Rev 2022;469:214684. https://doi.org/10.1016/j.ccr.2022.214684.

[9] Chen D, Zhong Z, Ma Q, Shao J, Huang W, Dong X. Aza-BODIPY-based nanomedicines in cancer phototheranostics. ACS Appl Mater Interfaces 2020;12:26914–25. https://doi.org/10.1021/acsami.0c05021.

[10] Kaur M, Janaagal A, Balsukuri N, Gupta I. Evolution of Aza-BODIPY dyes-A hot topic. Coord Chem Rev 2024;498:215428. https://doi.org/10.1016/j.ccr.2023.215428.

[11] Kowada T, Maeda H, Kikuchi K. BODIPY-based probes for the fluorescence imaging of biomolecules in living cells. Chem Soc Rev 2015;44:4953–72. https://doi.org/10.1039/c5cs00030k.

[12] Mao Z, Kim JH, Lee J, Xiong H, Zhang F, Kim JS. Engineering of BODIPY-based theranostics for cancer therapy. Coord Chem Rev 2023;476:214908. https://doi.org/10.1016/j.ccr.2022.214908.

[13] Bassan E, Gualandi A, Cozzi PG, Ceroni P. Design of BODIPY dyes as triplet photosensitizers: electronic properties tailored for solar energy conversion, photoredox catalysis and photodynamic therapy. Chem Sci 2021;12:6607. https://doi.org/10.1039/d1sc00732g.

[14] Wang D, Wang X, Zhou S, Gu P, Zhu X, Wang C, Zhang Q. Evolution of BODIPY as triplet photosensitizers from homogeneous to heterogeneous: the strategies of functionalization to various forms and their recent applications. Coord Chem Rev 2023;482:215074. https://doi.org/10.1016/j.ccr.2023.215074.

[15] Ma C, Zhang T, Xie Z. Leveraging BODIPY nanomaterials for enhanced tumor photothermal therapy. J Mater Chem B 2021;9:7318. https://doi.org/10.1039/d1tb00855b.

[16] Sun W, Zhao X, Fan J, Du J, Peng X. Boron dipyrromethene nano-photosensitizers for anticancer phototherapies. Small 2019;15:1804927. https://doi.org/10.1002/smll.201804927.

[17] El-Mashtoly SF, Gerwert K. Diagnostics and therapy assessment using label-free Raman imaging. Anal Chem 2022;94:120–42. https://doi.org/10.1021/acs.analchem.1c04483.

[18] Wang Y, Yan B, Chen L. SERS tags: novel optical nanoprobes for bioanalysis. Chem. Rev. 2013;113:1391–428. https://doi.org/10.1021/cr300120g.

[19] Jaworska A, Wojci T, Malek K, Kwolek U, Kepczynski M, Ansary AA, Chlopicki S, Baranska M. Rhodamine 6G conjugated to gold nanoparticles as labels for both SERS and fluorescence studies on live endothelial cells. Microchim Acta 2015;182:119–27. https://doi.org/10.1007/s00604-014-1307-5.

[20] Brem S, Schlucker S. Surface-enhanced Raman spectroscopy and density functional theory calculations of a rationally designed rhodamine with thiol groups at the xanthene ring. J Phys Chem C 2017;121:15310–7. https://doi.org/10.1021/acs.jpcc.7b01504.

[21] Javaid R, Sayyadi N, Mylvaganam K, Venkatesan K, Wang Y, Rodger A. Design and synthesis of boron complexes as new Raman reporter molecules for sensitive SERS nanotags. J Raman Spectrosc 2020;51:2408–15. https://doi.org/10.1002/jrs.6020.

[22] Chakraborty A, Ghosh A, Barui A. Advances in surface-enhanced Raman spectroscopy for cancer diagnosis and staging. J Raman Spectrosc 2020;51:7–36. https://doi.org/10.1002/jrs.5726.

[23] Adarsh N, Ramya AN, Maiti KK, Ramaiah D. Unveiling NIR aza-boron-dipyrromethene (BODIPY) dyes as Raman probes: surface-enhanced Raman scattering (SERS) - guided selective detection and imaging of human cancer cells. Chem Eur J 2017;23:14286–91. https://doi.org/10.1002/chem.201702626.

[24] Lu H, Mack J, Yang Y, Shen Z. Structural modification strategies for the rational design of red/NIR region BODIPYs. Chem Soc Rev 2014;43:4778–823. https://doi.org/10.1039/c4cs00030g.

[25] Quan L, Gu J, Lin W, Wei Y, Lin Y, Liu L, Ding H, Pan C, Xie Z, Wu T. A BODIPY biosensor to detect and drive self-assembly of diphenylalanine. Chem. Commun. 2019;55:8564–6. https://doi.org/10.1039/c9cc03810h.

[26] Quan L, Moreno-Gonzalez I, Xie Z, Gamez N, Vegas-Gomez L, Song Q, Gu J, Lin W, Gomez-Gutierrez R, Wu T. A near-infrared probe for detecting and interposing amyloid beta oligomerization in early Alzheimer's disease. Alzheimer's Dementia 2022:1–11. https://doi.org/10.1002/alz.12673.

[27] Presti D, Wilbraham L, Targa C, Labat F, Pedone A, Menziani MC, Ciofini I, Adamo C. Understanding aggregation-induced emission in molecular crystals: insights from theory. J Phys Chem C 2017;121:5747–52. https://doi.org/10.1021/acs.jpcc.7b00488.

[28] Wilbraham L, Louis M, Alberga D, Brosseau A, Guillot R, Ito F, Labat F, Métivier R, Allain C, Ciofini I. Revealing the origins of mechanically induced fluorescence changes in organic molecular crystals. Adv. Mater. 2018;30:1800817. https://doi.org/10.1002/adma.201800817.

[29] Yanai T, Tew DP, Handy NC. A new hybrid exchange–correlation functional using the Coulomb-attenuating method (CAM-B3LYP). Chem Phys Lett 2004;393:51–7. https://doi.org/10.1016/j.cplett.2004.06.011.

[30] Micheletti C, Wang Q, Ventura F, Turelli M, Ciofini I, Adamo C, Pucci A. Red-emitting tetraphenylethylene derivative with aggregationinduced enhanced emission for luminescent solar concentrators: a combined experimental and density functional theory study. Aggregate 2022;3:e188. https://doi.org/10.1002/agt2.188.

[31] Muniz-Miranda F, Minei P, Contiero L, Labat F, Ciofini I, Adamo C, Bellina F, Pucci A. Aggregation effects on pigment coatings: pigment red 179 as a case study. ACS Omega 2019;4:20315–23. https://doi.org/10.1021/acsomega.9b02819.

[32] M. J. Frisch, G. W. Trucks, H. B. Schlegel, G. E. Scuseria, M. A. Robb, J. R. Cheeseman, G. Scalmani, V. Barone, G. A. Petersson, H. Nakatsuji, X. Li, M. Caricato, A. V. Marenich, J. Bloino, B. G. Janesko, R. Gomperts, B. Mennucci, H. P. Hratchian, J. V. Ortiz, A. F. Izmaylov, J. L. Sonnenberg, D. Williams-Young, F. Ding, F. Lipparini, F. Egidi, J. Goings, B. Peng, A. Petrone, T. Henderson, D. Ranasinghe, V. G. Zakrzewski, J. Gao, N. Rega, G. Zheng, W. Liang, M. Hada, M. Ehara, K. Toyota, R. Fukuda, J. Hasegawa, M. Ishida, T. Nakajima, Y. Honda, O. Kitao, H. Nakai, T. Vreven, K. Throssell, J. A. Montgomery, Jr., J. E. Peralta, F. Ogliaro, M. J. Bearpark, J. J. Heyd, E. N. Brothers, K. N. Kudin, V. N. Staroverov, T. A. Keith, R. Kobayashi, J. Normand, K. Raghavachari, A. P. Rendell, J. C. Burant, S. S. Iyengar, J. Tomasi, M. Cossi, J. M. Millam, M. Klene, C. Adamo, R. Cammi, J. W. Ochterski, R. L. Martin, K. Morokuma, O. Farkas, J. B. Foresman, D. J. Fox, Gaussian, Inc, Wallingford CT, 2016..

[33] Dovesi R, Orlando R, Erba A, Zicovich-Wilson CM, Civalleri B, Casassa S, Maschio L, Ferrabone M, De La Pierre M, d'Arco P, Noël Y, Causà M, Rérat M, Kirtman B. CRYSTAL14: a program for the ab initio investigation of crystalline solids. Int J Quant Chem 2014;114:1287–317. https://doi.org/10.1002/qua.24658.

[34] Dovesi R, Erba A, Orlando R, Zicovich-Wilson CM, Civalleri B, Maschio L, Rérat M, Casassa S, Baima J, Salustro S, Kirtman B. Quantum-mechanical condensed matter simulations with CRYSTAL. Wiley Interdiscip Rev Comput Mol Sci 2018;8:e1360. https://doi.org/10.1002/wcms.1360.

[35] Duan C, Zhou Y, Shan G-G, Chen Y, Zhao W, Yuan D, Zeng L, Huang X, Niu G. Bright solid-state red-emissive BODIPYs: facile synthesis and their high-contrast mechanochromic properties. J Mater Chem C 2019;7:3471–8. https://doi.org/10.1039/c8tc06421k.

[36] Krishnan R, Binkley JS, Seeger R, Pople JA. Self-consistent molecular orbital methods. XX. A basis set for correlated wave functions. J Chem Phys 1980;72: 650–4. https://doi.org/10.1063/1.438955.

[37] Klintenberg M, Derenzo SE, Weber MJ. Accurate crystal fields for embedded cluster calculations. Comput Phys Commun 2000;131:120–8. https://doi.org/10.1016/S0010-4655(00)00071-0.

[38] Derenzo SE, Klintenberg MK, Weber MJ. Determining point charge arrays that produce accurate ionic crystal fields for atomic cluster calculations. J Chem Phys 2000;112:2074–81. https://doi.org/10.1063/1.480776.

[39] Polavarapu PL. Ab initio vibrational Raman and Raman optical activity spectra. J. Phys. Chem. 1990;94:8106–12. https://doi.org/10.1021/j100384a024.

[40] Keresztury G, Holly S, Besenyei G, Varga J, Wang A, Durig J. Vibrational spectra of monothiocarbamates-II. IR and Raman spectra, vibrational assignment, conformational analysis and ab initio calculations of S-methyl-N,N-dimethylthiocarbamate. Spectrochim Acta Mol Biomol Spectrosc 1993;49: 2007–26. https://doi.org/10.1016/S0584-8539(09)91012-1.

[41] Krishnakumar V, Keresztury G, Sundius T, Seshadri S. Density functional theory study of vibrational spectra and assignment of fundamental vibrational modes of 1-methyl-4-piperidone. Spectrochim Acta Mol Biomol Spectrosc 2007;68:845–50. https://doi.org/10.1016/j.saa.2006.12.069.

[42] Pagliai M, Osticioli I, Nevin A, Siano S, Cardini G, Schettino V. DFT calculations of the IR and Raman spectra of anthraquinone dyes and lakes. J Raman Spectrosc 2018;49:668–83. https://doi.org/10.1002/jrs.5334.

[43] Baker J. Molecular structure and vibrational spectra. In: Leszczynski J, editor. Handbook of computational chemistry. Dordrecht, The Netherlands: Springer; 2012. p. 293–359. https://doi.org/10.1007/978-94-007-0711-5_10.

[44] Arroyo IJ, Hu R, Merino G, Tang BZ, Peña-Cabrera E. The smallest and one of the brightest. Efficient preparation and optical description of the parent borondipyrromethene system. J Org Chem 2009;74:5719–22. https://doi.org/10.1021/jo901014w.

[45] Tram K, Yan H, Jenkins HA, Vassiliev S, Bruce D. The synthesis and crystal structure of unsubstituted 4,4-difluoro-4-bora-3a, 4a-diaza-s-indacene (BODIPY). Dyes Pigments 2009;82:392–5. https://doi.org/10.1016/j.dyepig.2009.03.001.

[46] Schmitt A, Hinkeldey B, Wild M, Jung G. Synthesis of the core compound of the BODIPY dye class: 4,4′-Difluoro-4-bora-(3a,4a)-diaza-s-indacene. J Fluoresc 2009; 19:755–8. https://doi.org/10.1007/s10895-008-0446-7.

[47] Dundas KOHM, Beerepoot MTP, Ringholm M, Reine S, Bast R, List NH, Kongsted J, Ruud K, Olsen JMH. Harmonic infrared and Raman spectra in molecular environments using the polarizable embedding model. J Chem Theor Comput 2021;17:3599–617. https://doi.org/10.1021/acs.jctc.0c01323.

[48] Torras J, Bromley S, Bertran O, Illas F. Modelling organic molecular crystals by hybrid quantum mechanical/molecular mechanical embedding. Chem Phys Lett 2008;457:154–8. https://doi.org/10.1016/j.cplett.2008.03.082.

[49] Pogonin AE, Postnikova DA, Shagurin AY, Belov DV, Usoltsev SD, Marfin YS. Macroheterocycles. Assignment of the vibrations of unsubstituted BODIPY and aza-BODIPY, vol. 14; 2021. p. 240–8. https://doi.org/10.6060/mhc213973p.

[50] Lee Y, Das S, Malamakal RM, Meloni S, Chenoweth DM, Anna JM. Ultrafast solvation dynamics and vibrational coherences of halogenated boron-dipyrromethene derivatives revealed through two-dimensional electronic spectroscopy. J Am Chem Soc 2017;139:14733–42. https://doi.org/10.1021/jacs.7b08558.

[51] Tikhonov SA, Sidorin AE, Ksenofontov AA, Kosyanov DY, Samoilov IS, Skitnevskaya AD, Trofimov AB, Antina EV, Berezin MB, Vovna VI. XPS and quantum chemical analysis of 4Me-BODIPY derivatives. Phys Chem Chem Phys 2023;25:5211–25. https://doi.org/10.1039/d2cp04541a.

[52] Sandoval JS, Gong Q, Jiao L, McCamant DW. Stimulated resonance Raman and excited-state dynamics in an excitonically coupled bodipy dimer: a test for TD-DFT and the polarizable continuum model. J Phys Chem A 2023;127:7156–67. https://doi.org/10.1021/acs.jpca.3c02978.

[53] Sandoval JS, McCamant DW. The best models of bodipy's electronic excited state: comparing predictions from various DFT functionals with measurements from femtosecond stimulated Raman spectroscopy. J Phys Chem A 2023;127:8238–51. 0.1021/acs.jpca.3c05040.

[54] Singh N, Kumar P, Riaz U. Applications of near infrared and surface enhanced Raman scattering techniques in tumor imaging: a short review. Spectrochim Acta Mol Biomol Spectrosc 2019;222:117279. https://doi.org/10.1016/j.saa.2019.117279.